Author Contributions:
Conceptualization: Aditya Narayanan
Data curation: Aditya Narayanan
Formal analysis: Aditya Narayanan
Investigation: Aditya Narayanan
Methodology: Aditya Narayanan, Sarah T. Gille, Matthew R. Mazloff, Marcel D. du Plessis, K. Murali, Fabien Roquet
Software: Aditya Narayanan
Validation: Aditya Narayanan
Visualization: Aditya Narayanan
Writing – original draft: Aditya Narayanan, Sarah T. Gille, Fabien Roquet

Zonal Distribution of Circumpolar Deep Water Transformation Rates and Its Relation to Heat Content on Antarctic Shelves

Aditya Narayanan[1] , Sarah T. Gille[2] , Matthew R. Mazloff[2] , Marcel D. du Plessis[1] , K. Murali[3], and Fabien Roquet[1]

[1]Department of Marine Sciences, University of Gothenburg, Gothenburg, Sweden, [2]Scripps Institution of Oceanography, University of California San Diego, La Jolla, CA, USA, [3]Indian Institute of Technology Madras, Chennai, India

Abstract We analyze 15-year of observational data and a 5-year Southern Ocean model simulation to quantify the transformation rates of Circumpolar Deep Water (CDW) and the associated heat loss to the surface. This study finds that over the continental shelves of East Antarctica and the Weddell and Ross Seas, surface buoyancy fluxes transform ∼4.4 Sv of surface waters into CDW, providing a path for CDW to lose heat to the surface. In addition, ∼6.6 Sv of CDW are mixed with surface waters in the Weddell and Ross subpolar gyres. In contrast, enhanced stratification inhibits the outcropping of CDW isopycnals, reducing their transformation rates by a factor of ∼8 over the continental shelf and by a factor of ∼3 over the deeper ocean in the Amundsen and Bellingshausen Seas. The CDW retains its offshore warm properties as it intrudes over the continental shelves, resulting in elevated bottom temperatures there. This analysis demonstrates the importance of processes in subpolar gyres to erode CDW and to facilitate further transformation on the continental shelves, significantly reducing the heat able to access ice shelf fronts. This sheltering effect is strongest in the western Weddell Sea and tends to diminish toward the east, which helps explain the large zonal differences in continental-shelf bottom temperatures and the melt rates of Antarctic ice shelves.

Plain Language Summary The continental slope around Antarctica acts as a barrier to deep and warmer offshore waters that can bring heat to the glaciers along the coastline, enhancing their melt rate and contributing to global sea level rise. Around the Antarctic continent these offshore waters, the so-called Circumpolar Deep Waters, differ in their ability to cross this barrier while retaining their heat, explaining to a large extent why West Antarctic glaciers melt much faster than other Antarctic ice sheets. We study the properties of the warm waters over the continental shelf and offshore regions and contrast them across regions. We show that in East Antarctica, the Ross Sea, and the Weddell Sea, deep warm waters are brought to the surface where they lose heat and mix with surface waters. However, in the Amundsen and Bellingshausen Seas, the warm water is insulated from the surface by land run-off of fresher and lighter waters that occupy the surface. These results highlight the importance of the subpolar gyres in sheltering Antarctic glaciers.

1. Introduction

Circumpolar Deep Water (CDW) is a relatively warm layer of water (∼1–2°C) that is part of the lower branch of the global overturning circulation (Talley, 2013). CDW upwells in the subpolar gyres of the Southern Ocean and mixes with surface waters, transforming into lighter watermasses (Pellichero et al., 2018). CDW can also shoal onto the Antarctic continental shelf where it may undergo mixing with shelf watermasses, transforming into heavier and cooler Dense Shelf Water (DSW with $\sigma_\theta \geq 27.86$ kg/m³; Orsi et al., 1999). In some regions of Antarctica, CDW does not undergo transformation as it flows onto the continental shelf, retaining its warmer offshore properties, thereby elevating the temperatures at the base of ice shelves along the coastline (Jenkins & Jacobs, 2008; Ribeiro et al., 2021).

Another prominent watermass that CDW can transform into, as it encounters coastal polynyas, is a cooler version of itself, called modified-CDW (mCDW; with $28 < \gamma^n < 28.27$ kg/m³; Williams et al., 2016). Along the ice shelf edge, mCDW has been found even in regions with a cold-cavity ice shelf, such as the Weddell Sea (Årthun et al., 2012), Prydz Bay (Williams et al., 2016), and the Ross Sea (Piñones et al., 2019). Though mCDW is a cooler watermass, it still remains warmer than the near-freezing waters formed on the continental shelves; hence it has the ability to elevate the melt rates of ice shelves (Adusumilli et al., 2020). Throughout the rest of this text,

Writing – review & editing: Aditya Narayanan, Sarah T. Gille, Matthew R. Mazloff, Marcel D. du Plessis, K. Murali, Fabien Roquet

we use the term "CDW" to encompass both CDW in its un-modified form as well as the cooler mCDW watermasses (see Section 2).

The Antarctic Slope Front (ASF; Heywood et al., 2004) that forms between the cold and dense watermasses on the continental shelf and the warmer and relatively lighter offshore CDW forms a dynamic barrier that restricts the access of warmer CDW to the continental shelf and to the base of the ice shelves (Thompson et al., 2018). However, intrusion of warm CDW across the ASF can drive the retreat of ice shelves via basal melting, leading to the retreat of the glaciers buttressed by the ice shelves (Jenkins & Jacobs, 2008), eventually affecting global climate and causing sea level rise (Hansen et al., 2016; Hillenbrand et al., 2017).

A variety of mechanisms can transport CDW onto the continental shelf. The interaction of the longshore mean flow with cross-slope troughs at the continental shelf break can channel CDW watermasses onto the continental shelf (Dinniman et al., 2011; St-Laurent et al., 2013). The Antarctic Circumpolar Current (ACC) makes its closest approach to the Antarctic continent along the continental shelf break in the Bellingshausen Sea, where the eastward bottom mean flow results in a coastward bottom Ekman transport (Gille et al., 2016). Offshore flow of shelf waters draws a compensatory shoreward flow of CDW (Lewis & Perkin, 1986). In regions where the predominant zonal winds over the continental slope are westerlies, CDW isopycnals are uplifted toward the slope, providing a pathway for CDW onshore intrusion (Chavanne et al., 2010). CDW is also transported across the dynamic barrier formed by the ASF via transient processes such as eddies spawned from hydrodynamic instabilities (Stewart & Thompson, 2015) and coastally trapped waves (Webb et al., 2019). CDW intrudes close to the ice shelves in the Amundsen and Bellingshausen Seas, elevating the basal melt rates of ice shelves leading to grounding line retreat of ice sheets (Jacobs et al., 2011; Petty et al., 2013; Rignot et al., 2013).

To further complicate matters, the eastward flowing Antarctic Slope Current (ASC; Thompson et al., 2018) can transport watermasses across marginal seas, which could enhance the convection and production of DSW (e.g., Cape Darnley; Ohshima et al., 2013), or could suppress the formation of dense waters by transporting freshwater (e.g., Western Ross Sea; Guo et al., 2020).

Previously held views on the Amundsen and Bellingshausen Seas were that these regions experienced warmer bottom temperatures as a result of enhanced rates of cross-slope CDW intrusion (Schmidtko et al., 2014; Thoma et al., 2008). However, model-based studies have found greater onshore volume and heat transport, not in the Amundsen and Bellingshausen Seas, but rather within the CDW layer in regions producing DSW overflows (Dinniman et al., 2011; Morrison et al., 2020). Tamsitt et al. (2021) used numerical models to show that though cold regions such as the Weddell and Ross Seas receive more CDW volume (and heat) influx over the continental shelf, this intrusion is not associated with higher continental shelf bottom temperatures because CDW has a lower residence time over the continental shelf in these DSW producing regions. They attributed this low residence time to CDW mixing with colder shelf waters and thereby losing heat to the atmosphere. Hence, quantifying the mixing that CDW undergoes is important, as it determines the ocean heat content along the Antarctic coastline. We leverage the watermass transformation framework to study the impact of CDW diapycnal mixing and surface fluxes on the heat content over the continental shelf and continental slope of Antarctica.

In this study, we quantify the time-mean state of the properties of CDW in the Southern Ocean and their watermass transformation rates, and we use these rates as an indicator of heat loss of the CDW layer. It is necessary to go beyond simple considerations of CDW flux across the continental slope. Hence we build a larger-scale perspective by studying how the properties of CDW are modulated by processes over the continental shelf and within subpolar gyres. We draw a contrast in CDW spatial properties between West and East Antarctica to explain the differences in continental shelf bottom temperature regimes.

2. Methods and Data

2.1. Observational Hydrography Data

Observational hydrographic data were obtained from the tagged marine seal data set (MEOP: Marine Mammals Exploring the Oceans Pole to Pole; Treasure et al., 2017), the Argo float data set (Argo, 2019), and under-ice Argo floats deployed as part of the Southern Ocean Carbon and Climate Observations and Modeling project (SOCCOM, 2019). All data south of 60°S have been used from the period 2004 to 2019. Floats and tagged seal vertical profiles are fairly well distributed over the continental shelf around Antarctica, and the discussion
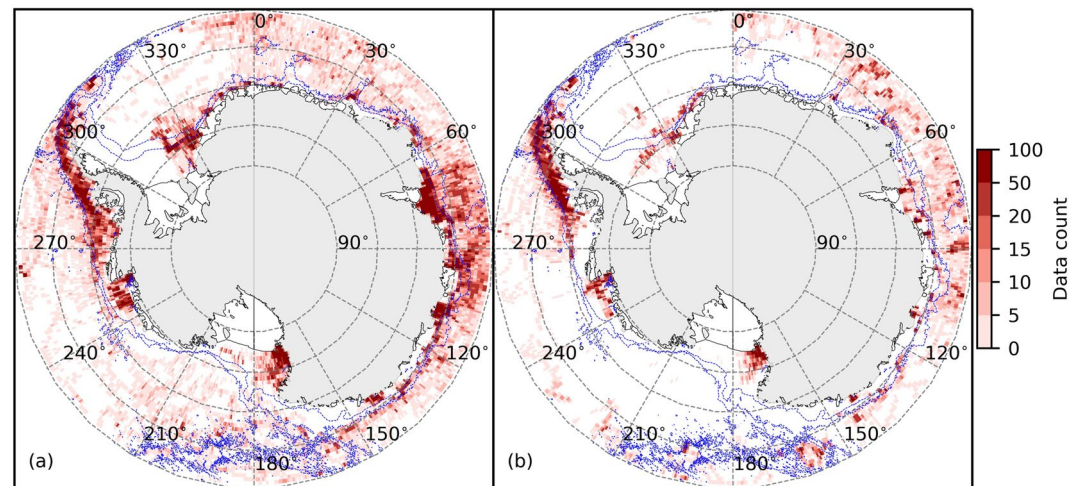
Figure 1. Profile count in (a) summer (December through May) and (b) winter (June through November) seasons aggregated in grid cells of $0.5° \times 0.5°$. Contour lines are drawn for the 1,000 and 3,000 m isobaths.

of observations throughout this article refers only to regions that are well sampled (Figure 1). Observations are heterogenous in both space and time, with different regions being sampled at different time periods. We rely on model-derived fields (described later in this Section) to discuss regions that have not been sampled by observing systems. The continental slope of the Ross Sea during winter is one such example. We point out such data gaps in our discussion of the results. The time average of the observational data is affected by the temporal sampling biases and does not represent the climatology of the region. Temporal sampling details are provided in the Supporting Information S1 (Figure S1), and these results need to be considered with caution in regions with low temporal sampling counts. However, at the moment, these datasets provide the widest coverage of the Southern Ocean and allow us to gain a novel perspective into processes.

The MEOP data undergo a post-calibration process, which involves quality control and corrections to the data based on historical CTD data available from the region sampled as well as by using cross-correlation techniques (Roquet et al., 2011). The tags transmit low-resolution data in the vertical using a broken stick method. In our analysis, we linearly interpolate the data to 2 m intervals between the data points in each profile. The interpolated data have an error of $\pm 0.04°C$ for temperature and ± 0.03 g kg^{-1} for salinity (Siegelman et al., 2019). The Argo floats also undergo real-time and delayed mode quality control tests (Wong et al., 2020), and only data flagged as good have been used in this study.

2.2. Numerical Model Data

To complement the observational data in evaluating the ocean properties, we use the SO12, a 1/12° resolution model simulation of the Southern Ocean circulation based on the MITgcm (Massachussets Institute of Technology general circulation model) and described earlier by Erickson et al. (2016).

In short, the SO12 model domain is circumpolar, ranging from 78°S to the equator, and it is restored toward the ECCOv4 solution (Forget et al., 2015) at the equator. The model uses z coordinates with partial cells (Adcroft et al., 1997) with 104 vertical levels that range from 2 m thick at the surface to 200 m thick at the ocean floor. Bathymetry is derived from ETOPO-1 (ETOPO1, 2009). The primitive equations are solved on an Arakawa C grid using a third-order direct space-time flux limiting advection scheme. The timestep is 300 s. Horizontal viscosity is parameterized using a modified Leith scheme (Fox-Kemper & Menemenlis, 2008). There is no explicit horizontal diffusivity. Vertical viscosity and diffusivity are parameterized using Gaspar et al. (1990), with a background diffusivity of 1×10^{-5} m^{2}s^{-1}. A quadratic bottom drag is prescribed with a drag coefficient of 0.002. Sea ice thermodynamics is evolved from Semtner (1976) as explained in Fenty and Heimbach (2013). Sea ice rheology is solved for using a Line Successive Over Relaxation scheme (LSOR; Zhang & Hibler, 1997).

The SO12 model is forced by atmospheric fluxes of heat, freshwater, and momentum calculated by boundary-layer bulk formulas (Large & Yeager, 2004) that used prescribed values for the atmospheric state from ERA-Interim

(Dee et al., 2011). This model was initialized in 2005 from a 1/6° resolution state estimate output (M. R. Mazloff et al., 2010). The first 12 months were considered as a spinup allowing the 1/12° model state (e.g., kinetic energy) to adjust from the 1/6° initial conditions. The diagnostics used in this analysis were computed from monthly averages for the period from January 2006 to December 2010. Because monthly averaged output was analyzed, our study does not consider high-frequency processes occurring at the time scale of hours or days. This model does not include tidal forcing, ice shelf cavities, or thermodynamic interactions. Melt rate and continental runoff are prescribed from Hammond and Jones (2016). As Stewart and Thompson (2012) note, the uncertainty in the bathymetry used in the model is high and may contribute to errors in the dynamics computed in this region. The resolution of this model is coarser than the Rossby radius of deformation over the continental shelf regions of the Southern Ocean; hence the hydrodynamics may not be fully represented. More details on the model configuration may be found in the Supporting Information S1.

2.3. Model Validation

Erickson et al. (2016) have validated the SO12 model versus observations in the Weddell Sea. We provide here complementary model–data comparisons. The SO12 model and observational data were binned into 0.5° × 0.5° bins over which the isopycnal surfaces corresponding to the CDW layer ($\sigma_\theta = 27.67, 27.74$ kg/m^3; see Section 2.4) were selected. For each selected isopycnal surface, we computed the time-averaged (across model run time for the SO12 model and across the 15-year period for the observations) depth and potential temperature.

The comparison between observed and SO12-produced properties of the top layer of CDW ($\sigma_\theta = 27.67$ kg/m^3) are shown in Figure 2 and for the core layer of CDW ($\sigma_\theta = 27.74$ kg/m^3) in Figure S2 in Supporting Information S1. We show difference plots (model less observations) in Figures S7 and S8 in Supporting Information S1. We also quantify the difference (neglecting grid cells without data in the observations) between the modeled fields relative to the observed fields using the mean averaged error (MAE) in Table 1. These results show a good agreement between the modeled and observed hydrography of the CDW layers discussed in the main text. In general, the biases in the model are toward deeper CDW isopycnals and warmer CDW with the largest warm bias in the Weddell Sea gyre region (Figure 2). The continental shelves in parts of East Antarctica too are warmer than the observed temperatures. Despite this bias, we still find that the cooler and shallower isopycnals are co-located across the model and observations. We caution here that the observations are sparse in this region and suffer from spatial and temporal sampling biases. Hence we are unable to compare the model with observations that truly represent the climatology of the region, and we are only able to offer a qualitative assessment of the model's performance.

Despite its potential shortcomings, the model provides a robust means to evaluate the evolution of large-scale water masses in the subpolar Southern Ocean and in the Antarctic marginal seas. The model is used in this study to analyze the distribution of CDW and how this distribution is affected by the general circulation, overturning, and interaction with convective activity over the continental shelf. The SO12 model, initialized from a state estimate, provides realistic fields, agrees well with in situ observations of CDW distribution, and is a useful tool for this analysis.

2.4. Water Mass Transformation Framework

Southern Ocean studies typically use neutral density (γ^n; Jackett & McDougall, 1997) to define watermasses (e.g., Iudicone et al., 2008). However, this study is focused on the upper 700 m of the ocean, where there is little difference between gradients of neutral and potential density. Potential density is used here since it is computationally easier to obtain and does not rely on regional look-up tables. Definitions of CDW most commonly found in the literature define the layer as lying between neutral densities of 28 and 28.27 kg m^{-3} (Williams et al., 2016). We follow Williams et al. (2016) in defining this watermass to encompass CDW in its unmodified form as found at depth, and in its modified and cooler form (mCDW). We do this to track the effects of watermass transformation on the heat content of this layer. We follow the procedure adopted by Abernathey et al. (2016) where they carried out their watermass transformation analysis using the potential density field, but converted their results into neutral densities using a linear curve fit. We do the same using the tagged seal data (see Figure S3 in Supporting Information S1) to convert from potential density values to neutral density values. Since we remain within the upper 700 m ocean in this analysis and within a narrow density range encompassing the CDW layer, the error in the curve fit between neutral densities and potential density is negligible.

We use the definitions of cold, intermediate, and warm bottom temperature regime regions, as defined in an earlier study (Narayanan et al., 2019; see Table S1 in Supporting Information S1 and Figure 3). For regions not
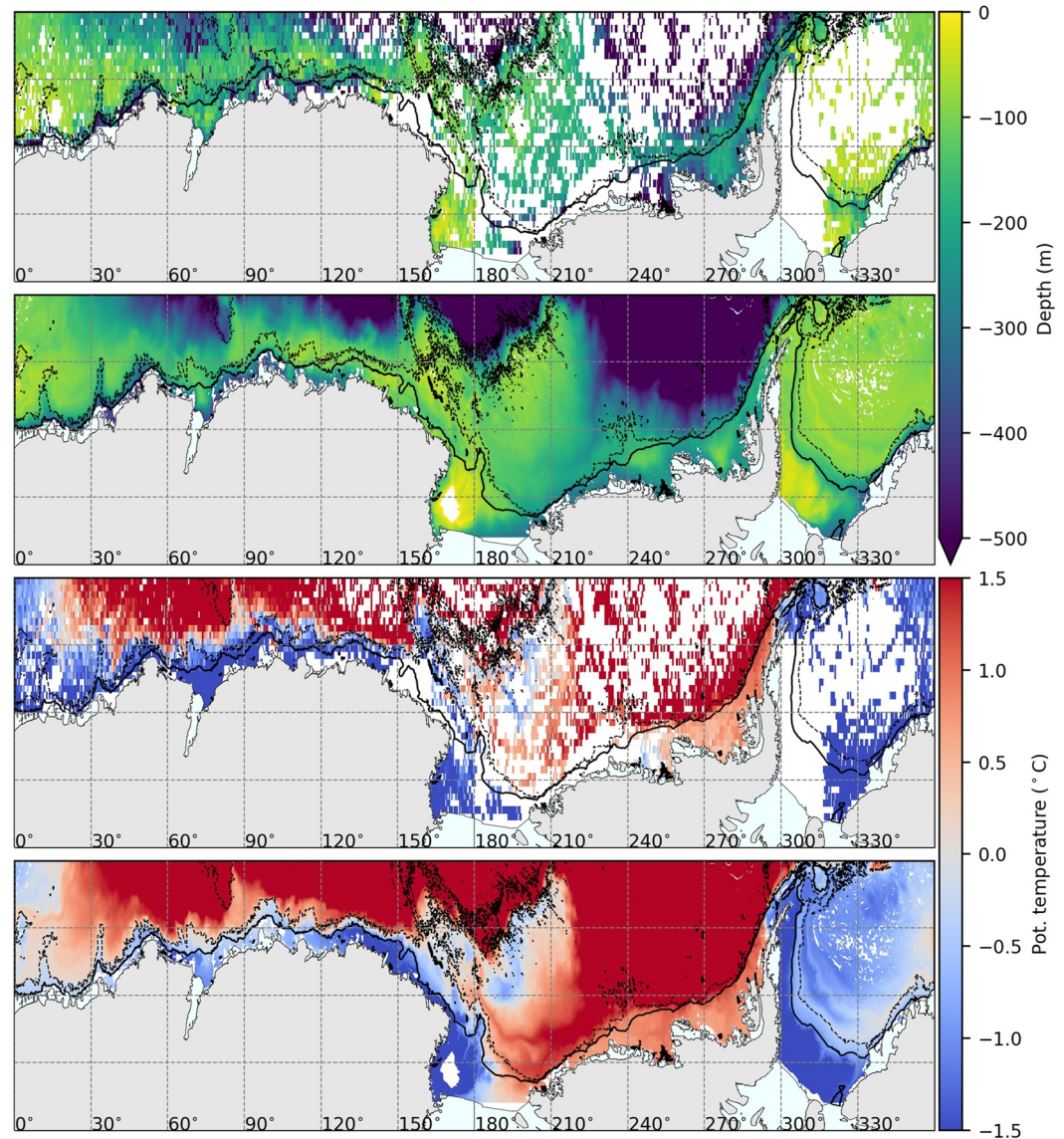
Figure 2. Comparison of Circumpolar Deep Water (CDW) top layer properties (σ_θ = 27.67 kg/m^3), with (a) observed depth, (b) modeled depth, (c) observed potential temperature, and (d) modeled potential temperature. See Figure S2 in Supporting Information S1 for CDW core layer properties (σ_θ = 27.74 kg/m^3).

Table 1
Mean Average Error (MAE = $\frac{\sum_{i=1}^{n} |y_i - x_i|}{n}$) Between Modeled ($y_i$) and Observed ($x_i$) Fields

Density class	Property	MAE			
		SO	WS	RS	AS & BS
27.67	Depth (m)	63	46	56	87
	Potential temperature (°C)	0.58	0.88	0.5	0.25
27.74	Depth (m)	85	64	67	102
	Potential temperature (°C)	0.6	1	0.37	0.21

Note. Regions shown above are the whole Southern Ocean (SO), Weddell Sea (WS; 300°–20° longitude), Ross Sea (RS; 160°–220° longitude), and the Amundsen and Bellingshausen Seas (AS & BS; 220°–300° longitude). (See Willmott and Matsuura (2005) for advantages of using MAE).
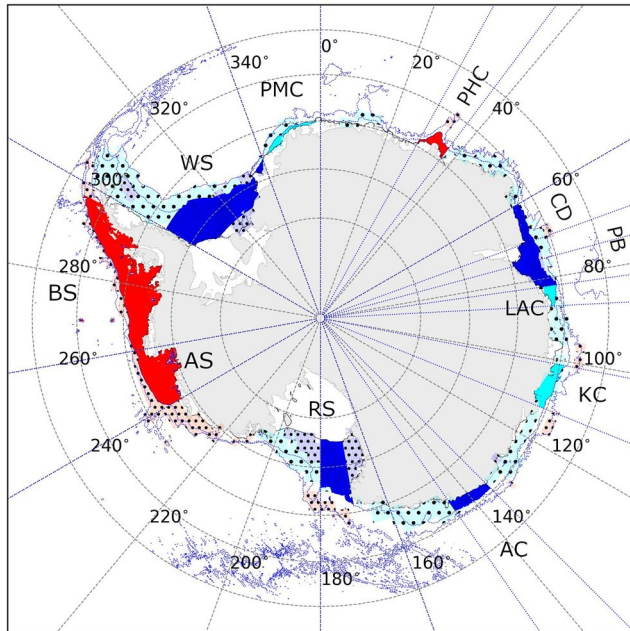
Figure 3. Summary of Narayanan et al. (2019) of the regional classification into cold, intermediate, and warm bottom temperature regimes (see Table S1 in Supporting Information S1). Here, blue color denotes regions where cold bottom temperatures were found, cyan indicates regions where intermediate bottom temperatures were found, while red indicates warm bottom temperatures. Lightly shaded regions with dot hatching show temperature regimes derived from the EN4.2.1 data set (see Section 2.4 in the main text; Good et al., 2013). Region names are abbreviated as WS, Weddell Sea; PMC, Princess Martha Coast; PHC, Prince Harald Coast; CD, Cape Darnley; PB, Prydz Bay; LAC, Leopold and Astrid Coast; KC, Knox Coast; AC, Adélie Coast; Ross Sea; AS, Amundsen Sea; and the BS, Bellingshausen Sea. Bathymetry contour lines show the 1,000 and 3,000 m isobaths.

included in the earlier study, we used the Hadley Centre's EN4.2.1 data set (quality controlled subsurface objective analyses; Good et al., 2013) over the period 2004 to 2020 to derive average continental shelf bottom temperatures (data below 270 m) to categorize regions as cold ($\overline{\theta} < -0.5$℃), intermediate (-0.5℃ $< \overline{\theta} < 0.5$℃) and warm ($\overline{\theta} > 1$℃) bottom temperature regimes (seen as lightly shaded regions in Figure 3). The objectively analyzed fields were developed using profiles obtained by a range of observational platforms, including tagged seals, Lagrangian floats, and ship-based observations.

The two isopycnal surfaces considered here correspond to potential densities (σ_θ, at reference pressure of 0 dbar, and reported as anomalies from 1,000 kg m^{-3}) of 27.67 and 27.74 kg m^{-3}. We consider $\sigma_\theta = 27.67$ kg m^{-3} (corresponding to a neutral density of $\gamma^n = 28.00$ kg m^{-3}) as the top of the CDW layer and $\sigma_\theta = 27.74$ kg m^{-3} (corresponding to $\gamma^n = 28.10$ kg m^{-3}) to lie within the core of the CDW layer. We calculate transformation rates for all densities, with each discretized to have a defined thickness of ± 0.01 kg m^{-3}.

Offshore CDW properties may vary across regions, hence making the choice of representative CDW isopycnals across the entire Southern Ocean challenging (Whitworth et al., 1998). Figure S8 in Supporting Information S1 tracks the density of the surface with maximum temperature below the surface (waters deeper than 100 m and shallower than 700 m) over the offshore regions of the Southern Ocean (seabed deeper than 3,000 m). This layer of CDW is unaffected by seasonal change (Whitworth et al., 1998). Offshore CDW at depth is densest in the Weddell Sea and lightest in the Amundsen and Bellingshausen Seas. The isopycnals considered in this analysis are lighter than the CDW layer shown in Figure S8 in Supporting Information S1. Our choice of the upper surface of CDW could include Antarctic Surface Waters (AASW) (seasonally varying watermass at the surface; (Park et al., 1998)), but this choice is necessary as our intention is to track the mixing of CDW with surface waters. We elaborate further on the implication of this choice in Section 3.2. We note here that we do not use temperature and salinity tracers to categorize watermasses, and the discussion of CDW throughout this text refers to the density classes defined here.

Watermass transformation rates, which represent the volume of waters lighter than σ becoming denser than σ (e.g., Groeskamp et al., 2019), are defined as:

$$\Omega = \frac{\partial}{\partial \sigma} \iiint \left(\frac{D\sigma}{Dt} \right) dV, \tag{1}$$

where $D\sigma/Dt$ represents the total derivative of density, sum of surface flux and interior diffusive contributions. Effectively, watermass transformation rates are a measure of the diapycnal volume flux across a given isopycnal: $\int u^{\mathrm{dia}} \cdot \hat{n} dA$. Where u^{dia} is the diapycnal velocity, $\hat{n}$ is the unit normal to the selected isopycnal (positive in the direction of increasing density), and A is the surface area of the isopycnal. The discretized form of Equation 1 used to diagnose model outputs is presented in Appendix A.

The watermass transformation due to surface fluxes $\Omega_{\mathrm{surface}}$ is obtained considering density changes due to net heat and freshwater surface fluxes,

$$\left(\frac{D\sigma}{Dt} \right)_{\mathrm{surface}} = -\alpha \frac{Q}{C_p \Delta z} + \beta \frac{S_0 (E - P)}{\Delta z}. \tag{2}$$

Here, α is the coefficient of thermal expansion, Q is the downward heat flux per unit area, C_p is the specific thermal heat capacity of seawater, β is the coefficient of haline contraction, S_0 is the surface salinity, $E - P$ is the rate of evaporation minus precipitation, and Δz is the fractional height of the surface grid cell.

Watermass transformation calculations are restricted to the upper 700 m of the water column, as the analysis is aimed at understanding CDW heat exchange with surface waters and the atmosphere. The surface grid cell

component of the watermass transformation rate accounts for surface heat and salinity fluxes, and the residual is considered as the internal mixing component.

We use the complex maximum covariance analysis (MCA) using the open-access Python library provided by Rieger et al. (2021). MCA is used to identify spatial patterns of co-variability between watermass transformation and ocean heat content (vertically averaged in the upper 500 m layer). The technique relies on using Hilbert transforms to capture phase shifts, hence accounting for time-lagged patterns of co-variability. We present results for the first mode as normalized spatial and temporal amplitudes that represent the maximum amount of the co-variability field.

In this analysis, we refer to the "surface layer," defined as the upper 150 m of the water column, which corresponds to the depth of the mean winter mixed-layer depth (MLD) within the coastal regions associated with DSW production (Figure S5 in Supporting Information S1). The MLD is computed as the depth at which the maximum stratification is attained above the pycnocline.

3. Subpolar Distribution of CDW and Its Transformation Rate

3.1. Spatial Distribution of CDW

The CDW layer shoals close to the surface within the subpolar gyres (Jullion et al., 2014), and in some regions, CDW shoals toward the continental slope (Stewart & Thompson, 2012), allowing easy access onto the continental shelf for CDW watermasses. CDW that crosses the continental slope may undergo watermass transformation on the continental shelf through mixing or due to diapycnal fluxes at the surface, changing its temperature and salinity, and in effect, lowering its heat content. In continental shelf regions where CDW does not undergo transformation, it is able to retain its warmer offshore temperatures as it approaches the base of the ice shelves, hence enhancing basal melt rates in these regions (Morrison et al., 2020).

We create spatial maps of the properties of two density classes corresponding to the top of the CDW layer ($\sigma_\theta = 27.67$ kg m^{-3}) and the core of the CDW layer ($\sigma_\theta = 27.74$ kg m^{-3}). We study how these properties vary across two different parts of the ocean, (a) the offshore subpolar region, and (b) the continental shelf (selected for bathymetry shallower than a 1,000 m, and using latitude bounds; see Supporting Information S1 for more details). We contrast the Amundsen and Bellingshausen Seas against the rest of the Southern Ocean. To capture the effect of watermass transformation, we use the term "CDW" to encompass both the unmodified CDW waters found at depth, as well as mCDW that cools as it intrudes onto the continental shelves (see Section 2.4). This allows us to track changes occurring on isopycnals, to build spatial maps of CDW transformation pathways, and to build spatial maps of CDW transformation pathways as these isopycnals intrude onto the continental shelves.

In the offshore subpolar regions of East Antarctica, and in the Ross and Weddell Seas, the observed mean depths of the CDW isopycnals lie within the "surface layer" (upper 150 m; see Section 2.4) of the water column (Figures 4a and 5a). The locations where CDW is present in the surface layer agree well across observations and the SO12 model output (red contour lines; Figures 4a and 5a).

In contrast, in the Amundsen and Bellingshausen Seas, CDW remains below the surface, although it is shallower than at mid-latitudes (Figures 4a and 5a). We see that CDW is cooler and fresher in regions where it outcrops into the surface layer, as it interacts with surface waters and the atmosphere. But in regions where it does not upwell or outcrop into the surface layer, its properties are more typical of unmodified mid-depth CDW (Figures 4 and 5b). Our results are consistent with the upwelling of CDW in the cyclonic subpolar gyres (Jullion et al., 2014) and with the upwelling associated with the meridional overturning circulation that is a part of the ACC system (Olbers et al., 2004).

We note here that our definition of the top surface of the CDW layer may encompass AASW as well. Regions with salinities lower than 34.5 PSU may include AASW within the density class of 27.67 kg/m^3. This is especially true within the Weddell Gyre (Figure 4c) where the freshest waters are seen. But this is necessary as our intention is to track the mixing between these two watermasses as we demonstrate in the following section. We rely on the denser isopycnal of 27.74 kg/m^3 to obtain properties of CDW that are relatively isolated from the influence of AASW. This interpretation is justified by the more saline waters seen on this isopycnal (Figure 5c).

3.2. CDW Watermass Transformation

The time-mean (over duration of the model run) watermass transformation rates for the top layer of CDW ($\sigma_\theta = 27.67$ kg m^{-3}; Figures 4d and 4e) and for the core of the CDW layer ($\sigma_\theta = 27.74$ kg m^{-3}; Figures 5d
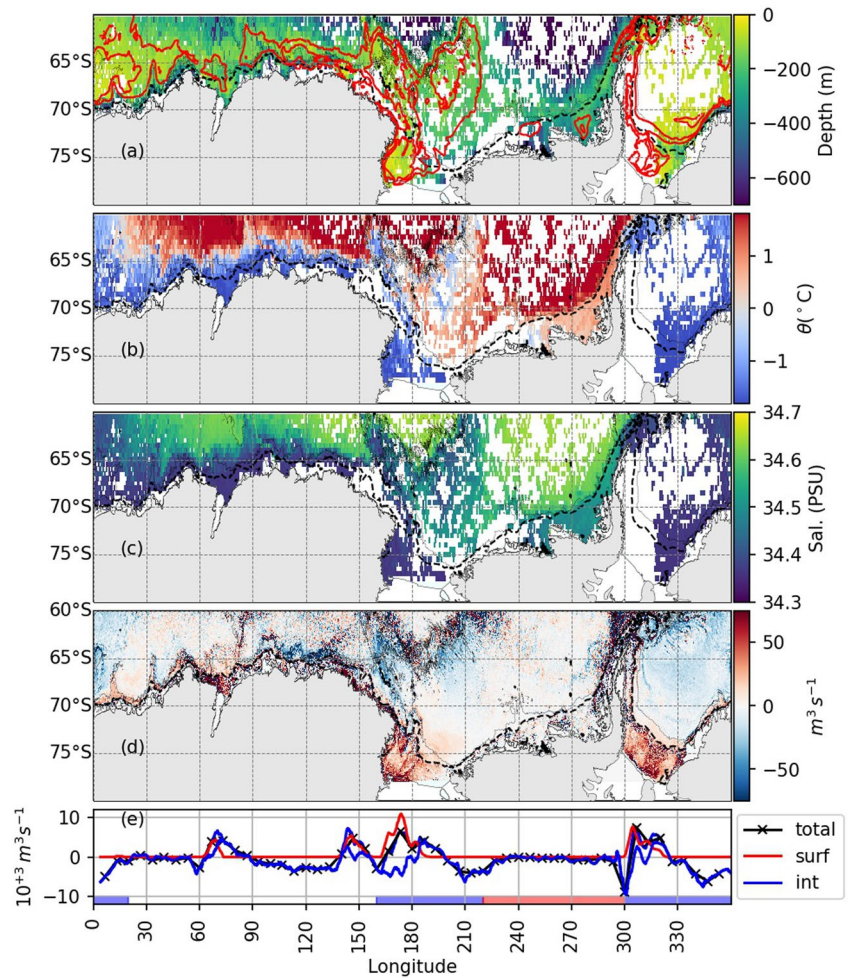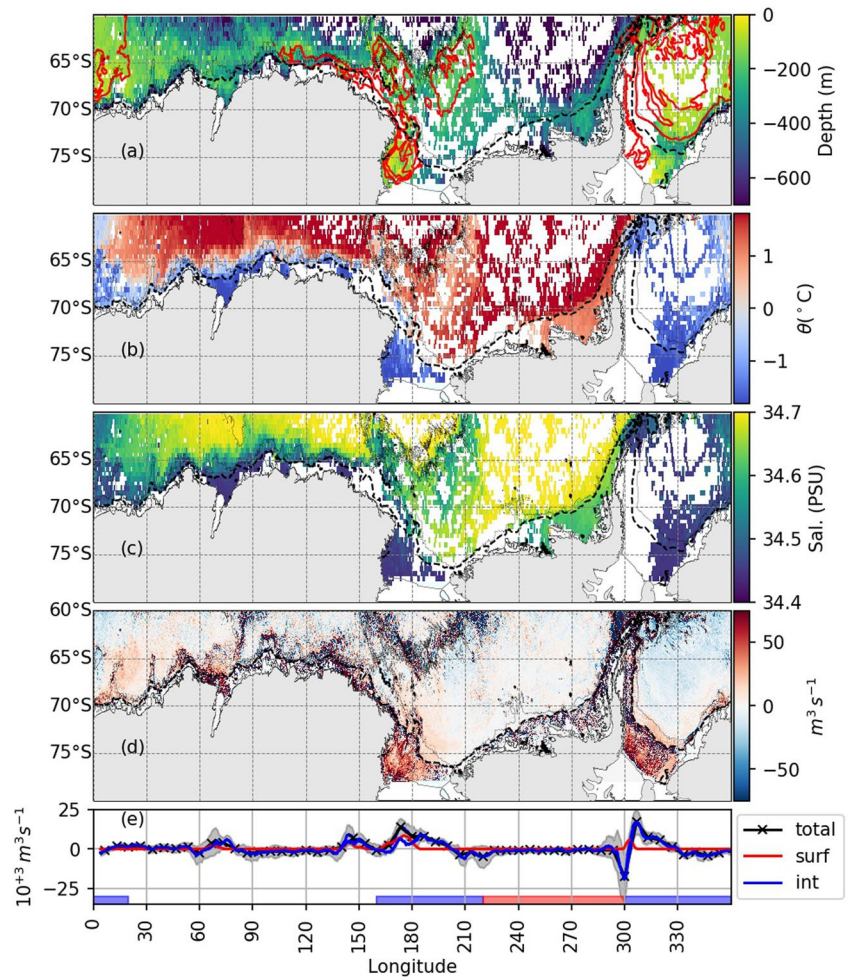
Figure 4. Circumpolar Deep Water (CDW) top layer properties ($\sigma_\theta = 27.67$ kg m^{-3}): (a) Observed depth (red contour lines enclose areas where modeled CDW layer is present in the upper 150 m of the water column), (b) observed potential temperature, (c) observed salinity, (d) time-mean watermass transformation rate, and (e) watermass transformation rate (for $\sigma_\theta = 27.67$ kg m^{-3}) summed meridionally for regions south of 60°S showing total, surface, and internal components (with the gray curve showing ±1 standard deviation around the total). Colored bands at the bottom indicate the Weddell Sea (blue band; 300°–30°), Ross Sea (blue band; 160°–220°), and the Amundsen and Bellingshausen Seas (red band; 220°–300°). All the maps show the 1,000 m (dark dashed line) and 3,000 m (light dashed line) isobath contour lines.

and 5e) are presented as volume flow rates in Sverdrups (10^6 m^3 s^{-1}), as they are measures of the volume of water transforming from lighter to denser water masses across the selected isopycnal (see Section 2.4). We also present them as volume per unit area within the text, with units of m s^{-1}. Negative values indicate waters heavier than the selected isopycnal transforming into waters lighter than the selected isopycnal. In assessing watermass transformation rates, we distinguish between processes that occur offshore and processes that occur over the continental shelf.

Over the offshore regions of the subpolar Southern Ocean (regions deeper than 3,000 m) of East Antarctica, the Weddell and Ross Seas, transformation rates of $\sigma_\theta = 27.67$ kg m^{-3} indicate buoyancy gain at rates $\approx -1.7 \times 10^{-7}$ m s^{-1}, indicating that the CDW top layer transforms into lighter watermasses, consistent with the idea that upwelled CDW mixes with surface waters (watermass transformation rates from Figure 4d; presented in per unit area terms). In contrast, in the Amundsen and Bellingshausen Seas, the transformation rate of $\sigma_\theta = 27.67$ kg m^{-3} is nearly 1/3rd as large (spatial mean of transformation rates between longitudes 220° and 300° $\approx -5.3 \times 10^{-8}$ m s^{-1}).

Over the continental shelf regions along East Antarctica and the Weddell and Ross Seas, transformation of $\sigma_\theta = 27.67$ kg m^{-3} is positive (buoyancy loss $\approx +3.5 \times 10^{-7}$ m s^{-1}; Figure 4d presented in per unit area terms),

Figure 5. Properties of the core of the Circumpolar Deep Water layer (σ_θ = 27.74 kg m^{-3}), presented as in Figure 4.

indicating that lighter watermasses are transformed into heavier density class watermasses, consistent with the idea that sea ice production in these regions results in salinification of surface waters, setting up vertical overturning and production of denser shelf watermasses. The surface flux enabled watermass transformation (red curve in Figures 4e and 5e) is only seen in the Prydz Bay, the Weddell Sea, and the Ross Sea. These are regions of strong coastal polynya activity where intruding CDW is transformed into denser and cooler DSW (Williams et al., 2016). Tamsitt et al. (2021) show that the coastal overturning and production of DSW is associated with very short residence times for CDW watermasses in these regions (about 50–200 days), as they are quickly transformed into heavier and cooler watermasses.

In contrast, over the continental shelves of the Amundsen and Bellingshausen Seas, CDW does not outcrop at the surface, and transformation remains negative at $\sim -0.4 \times 10^{-8}$ m s^{-1} (Figure 4d; presented as volume per unit area), which is 1/8th the magnitude elsewhere over the continental shelf. These regions do not produce DSW, and intruding CDW watermasses gain access to the base of the ice shelves without undergoing any mixing. Tamsitt et al. (2021) show that the mean residence time in these regions is about 350–600 days and is associated with greater bottom temperatures.

The Weddell Gyre (~ -3 Sv for σ_θ = 27.67 kg m^{-3}; between longitudes 300° and 20°; Figure 6b) and Ross Gyre (~ -1.8 Sv for σ_θ = 27.67 kg m^{-3}; between longitudes 160° and 220°; Figure 6b) are regions where the most upwelling and modification of CDW properties are seen (Figures 4d and 6a), with the CDW transformation in the Weddell Gyre being the feature that is largest in area with the strongest cooling and freshening. The total sum of CDW (σ_θ = 27.67 kg m^{-3}) transformation over the continental shelves ($\sim +4.4$ Sv) and over the deeper ocean
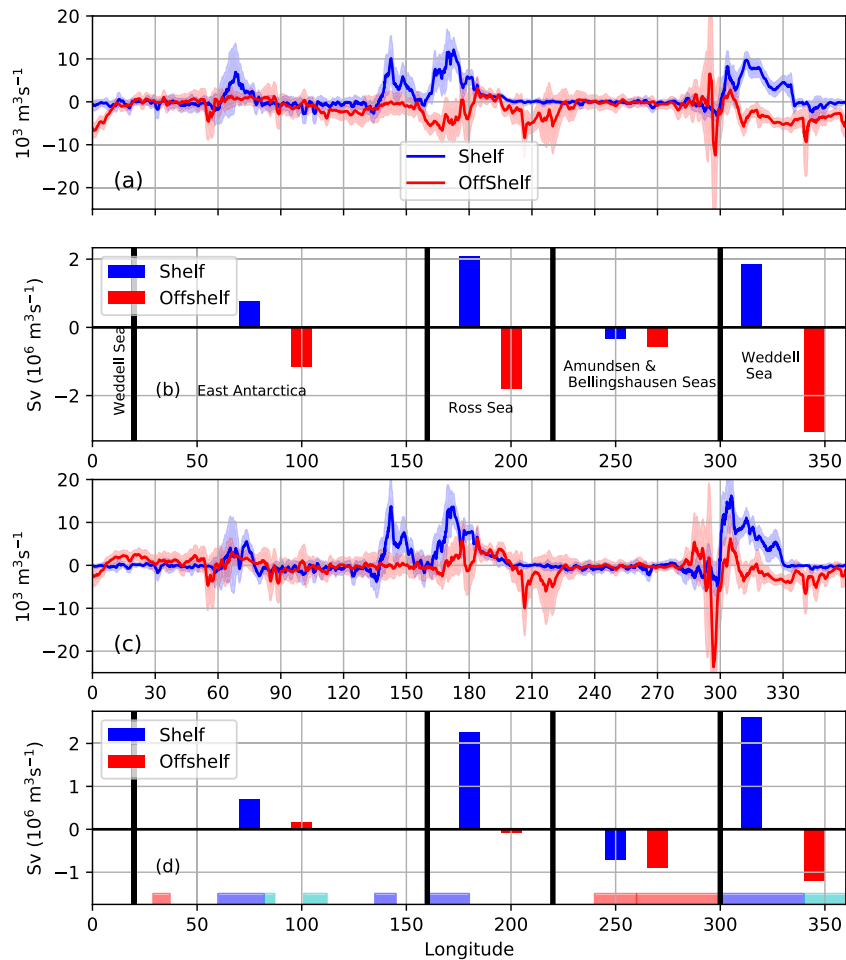
Figure 6. Time-mean (over model run time) Circumpolar Deep Water (CDW) transformation, meridionally integrated for (a) Top layer of CDW ($\sigma_\theta = 27.67$ kg m^{-3}), (b) Regional sum of (a) in Sv, (c) core layer of CDW ($\sigma_\theta = 27.74$ kg m^{-3}), (d) and its regional sum in Sv. Blue curve represents transformation over the continental shelf (shallower than 1,000 m) and the red curve is over the offshore regions. The lightly shaded area indicates ± 1 standard deviation. The colored bands at the bottom indicate continental shelf bottom temperature regimes as in Figure 3: warm (red), cold (blue), and intermediate (cyan). The dark vertical lines in (b) and (d) indicate regional bounds, names are shown in panel (b).

gyres (~ -6.6 Sv) is comparable (Figure 6a), indicating that both of these areas are important in causing heat loss from the CDW layer.

We infer that in the first case, over the open ocean gyres (Figures 6a and 6b; red curves), the upwelled CDW that is brought closer to the surface experiences enhanced rates of internal diapycnal mixing, becomes more buoyant, and is able to mix with surface waters, providing a path for CDW to lose heat to the surface. In the second case, over the continental shelves (Figures 6a and 6b; blue curve), surface buoyancy fluxes and internal mixing act together to make surface waters heavier, bringing them into the same density class as CDW, enabling the mixing between these two layers, once again providing a path for CDW to lose heat to the surface. This is mainly led by winter-time buoyancy loss in coastal regions (Figure S4c in Supporting Information S1). Either case allows more mixing, and in this particular domain, it happens that both modification scenarios result in cooler CDW. The relative extent of cooling and freshening ultimately determines if there is buoyancy gain or loss (see Figure 7 for an illustration of this effect).

Since both positive and negative transformation result in cooling, we compute the Pearson correlation coefficient r between the absolute magnitude ($|\Omega|$) of the annually averaged watermass transformation rate (averaged meridionally for the whole domain south of 60°S) and the annually averaged continental shelf (shallower than 1,000 m bathymetry) bottom temperature (averaged meridionally and between depths of 500 m to 1,000 m). Here r is
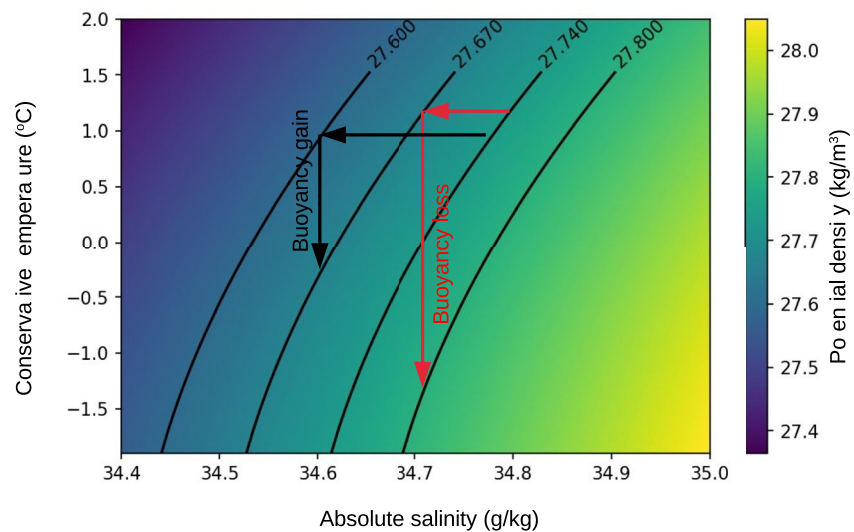
Figure 7. Illustration showing how freshening and cooling can lead to buoyancy gain (black pathway) or buoyancy loss (red pathway). The black contour lines are of potential density, σ_θ.

−0.358 [−0.380, −0.330] for the top layer of CDW (σ_θ = 27.67 kg m^{-3}) and −0.420 [−0.447, −0.398] for the core of the CDW isopycnal (σ_θ = 27.74 kg m^{-3}). The numbers in square braces denote the 95% confidence interval, computed using the effective sample size accounting for auto-correlations (Bretherton et al., 1999).

Hence, regardless of the sign of the watermass transformation rate, transformation is always associated with a cooling and freshening, in both the CDW top and core layer. We note here that the r values obtained above are statistically different from 0 and are noteworthy despite having low values. When it comes to such a complex system with multiple other factors that can influence the heat transport and surface heat flux, it is common to obtain rather low correlation coefficients even when a relation exists. But, in order to better quantify the connection between CDW transformation and ocean heat content, we analyze the spatial patterns of co-variability between these two fields.

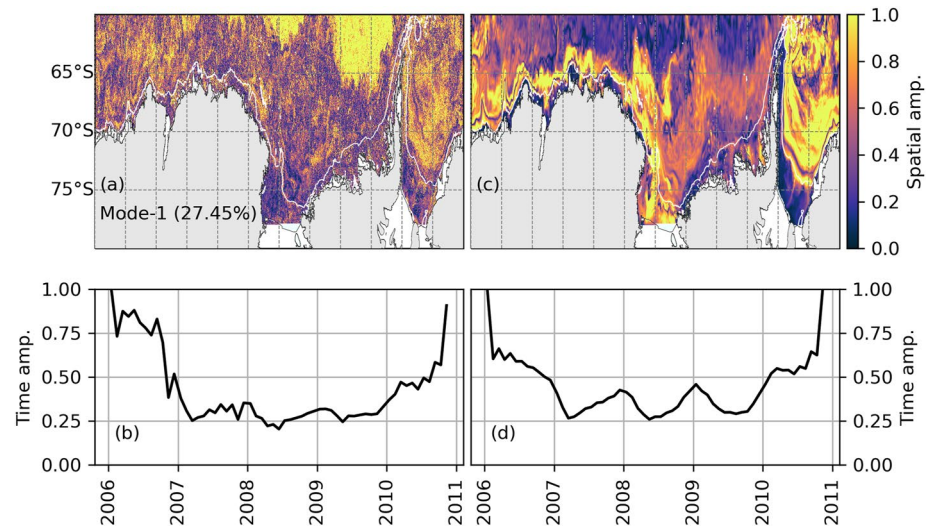### 3.3. Co-Variance of CDW Watermass Transformation and Ocean Heat Content

Correlations hide the spatial patterns of co-variability. We derive this by carrying out a complex MCA (see Section 2; Rieger et al., 2021) between the watermass transformation on the σ_θ = 27.67 kg/m^3 isopycnal with the ocean heat content in the upper 500 m layer (Figure 8). The first mode captures about 27% of the covariability between the two fields. Regions where the heat content shows high co-variability with watermass transformation are found over the Weddell Gyre, Ross Gyre, the continental slope of the Weddell and Ross Seas and along the continental slope of East Antarctica (Figure 8c). The Amundsen and Bellingshausen Seas show lower variability in heat content that co-varies with the watermass transformation field.

The spatial pattern of variability for the watermass transformation field shows larger amplitudes over the Weddell Gyre, Ross Gyre, and large parts of East Antarctica. A region of high variability is also found further north (latitude > 65°S) in the Ross Sea and the Bellingshausen Sea (Figure 8a). We infer that this is due to this region experiencing meandering in the ACC current. But this is not a region of high watermass transformation as we saw earlier (Figures 4 and 5d), which explains why there is no associated large variability in the heat content over this region as seen in Figure 8c.

Note here that this analysis shows the spatial patterns of co-variability, but does not establish the mechanistic links. We rely on our earlier analysis in Sections 3.1 and 3.2 to infer the physical mechanisms linking CDW watermass transformation and the resulting spatial distribution in CDW hydrography.

3.4. Links With Stratification

To identify the reason behind the zonal variation in watermass transformation, we look at the role of the stratification of the upper ocean, which is more strongly stratified over the continental shelf, continental slope, and the

Figure 8. Complex rotated maximum covariance analysis between watermass transformation (WMT; left field) on $\sigma_\theta = 27.67$ kg/m^3 isopycnal and the upper 500 m ocean heat content (OHC; right field). Normalized spatial amplitude of (a) WMT mode-1, (c) OHC mode-1. Normalized temporal amplitude of (b) WMT mode 1, (d) OHC mode 1. The 1,000 m isobath is plotted as a white line. Explained variance by mode-1 is 27.45%.

subpolar offshore regions in West Antarctica, whereas, the stratification is markedly weaker in East Antarctica and the Weddell and Ross Seas (time mean stratification of the upper 500 m water column computed as the difference between potential density at the surface and 500 m depth; Figure 9a).

The intrusion of warm unmodified CDW onto the continental shelf elevates the basal melt rate of ice shelves (Jacobs et al., 2011). This freshwater input can stratify the region, preventing deep convection and formation of DSW (Ribeiro et al., 2021). This highlights the two-way coupled nature of CDW–DSW interactions. Intrusion of unmodified CDW can suppress the formation of DSW, which in turn supports the onshore transport of more unmodified CDW in a positive feedback loop (Silvano et al., 2018).

Regions with stronger stratification are associated with higher net freshwater fluxes along the coastline and in the offshore subpolar region (Figure 9b) and higher glacial freshwater runoff fluxes (estimates of ice shelf and glacial runoff by Hammond and Jones (2016) were prescribed in this model; Figure 9c). The correlation between the time-averaged absolute magnitude of stratification over the continental shelf and slope and: (a) the time-averaged depth of the top layer of CDW is 0.338 [0.335, 0.340]; and (b) with the time-averaged depth of the core CDW isopycnal is 0.302 [0.300, 0.305]. (Again the numbers in square braces denote the 95% confidence interval.) This is consistent with the hypothesis that the stronger stratification due to higher freshwater flux from the land in West Antarctica (Figure 9c) inhibits the upwelling of CDW to the surface layer, thereby reducing the transformation and cooling of CDW before it arrives at the base of the ice shelves along the coastline.

We note here that the SO12 model prescribes the glacial freshwater runoff from the Hammond and Jones (2016) data set. Although we infer that CDW contributes to enhanced ice shelf melting, this model cannot be used to establish this causal link as it lacks ice shelf cavities.

4. Conclusions

Our analysis, using both in-situ observations collected across 15 years and a high-resolution Southern Ocean model, has investigated the CDW properties over the continental shelf and the subpolar regions in the context of the prevailing processes in these regions. Figure 10 summarizes the key processes identified in this study.

We have shown that CDW undergoes large transformations in the subpolar gyres of East Antarctica, and the Weddell and Ross Seas, aided by weaker stratification in the upper 500 m water column, resulting in lower heat content reaching the continental shelf break. The CDW outcrops at a shallower depth over the continental shelf in regions with shelf water overflows. This outcropping is accompanied by a loss in heat and salinity that
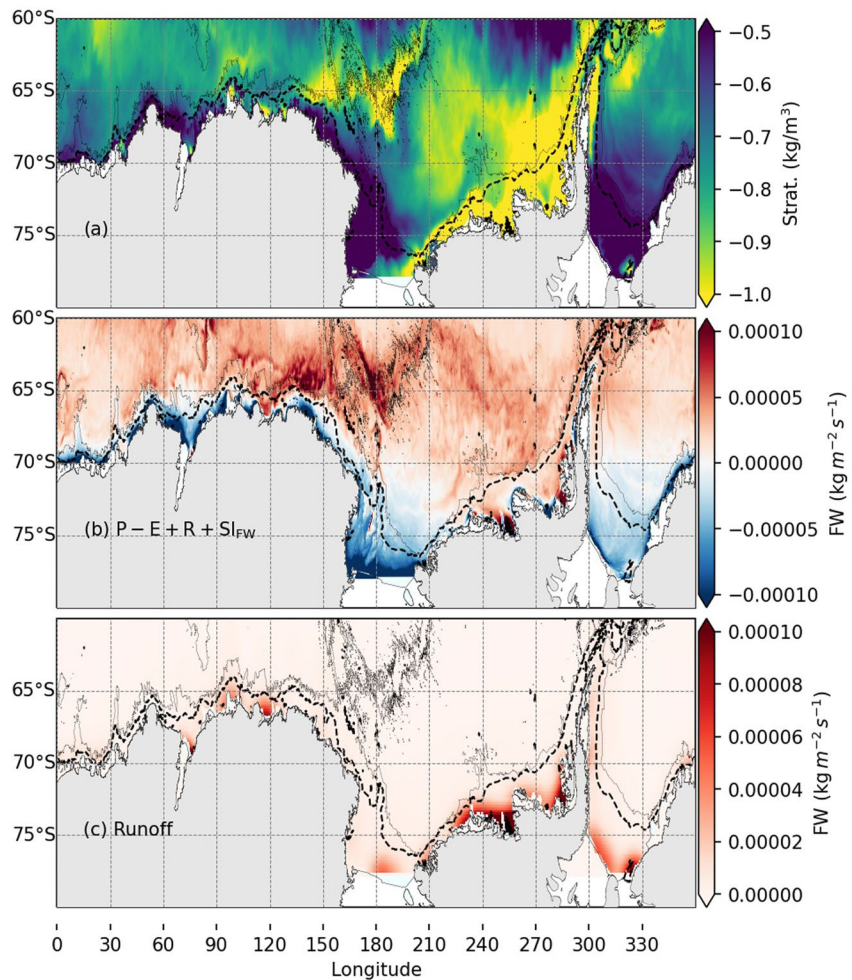
Figure 9. From SO12 model: (a) vertically integrated annual-mean stratification, (b) time-mean net surface freshwater flux (including precipitation (P), evaporation (E), land runoff (R), and sea ice (SI_{FW})), and (c) land runoff.

is associated with a relatively high watermass transformation rate ∼8 times greater than the CDW-top-layer transformation rate inferred over the Amundsen and Bellingshausen continental shelves. CDW upwells in the Amundsen and Bellingshausen Seas as well, but is blocked from reaching the surface layer by the stronger stratification in these regions. Stronger stratification is found in regions where DSW does not form and where higher freshwater fluxes are found along the coast.

Regions with CDW upwelling to the surface layer in the subpolar regions or with CDW outcropping into the surface layer over the continental shelf are also regions that experience cooler continental shelf bottom temperatures. The correlation between the CDW isopycnal depth (averaged in time and meridionally for the whole domain south of 60°S) and the time-averaged bottom temperature (averaged meridionally and between depths of 500–1,000 m) is significant over the continental shelf (shallower than 1,000 m bathymetry), with correlation coefficients of 0.54 [0.52, 0.56] for the top layer of CDW and 0.53 [0.5, 0.55] for the core of the CDW layer. Spatial patterns of co-variability revealed by a MCA confirmed that the ocean heat content is affected by CDW watermass transformation in regions where watermass transformation is large. In the Amundsen and Bellingshausen Seas, ocean heat content co-varies less strongly with CDW transformation, indicating that the heat content is weakly impacted by CDW transformation (if at all).

The CDW watermass transformation rates over the continental shelves and over the open ocean gyres are of similar magnitude but opposite signs. Regardless of the sign, in both cases, transformation results in lower temperatures and salinities as seen in the spatial maps in Figures 4 and 5. This shows that the heat loss pathways of CDW
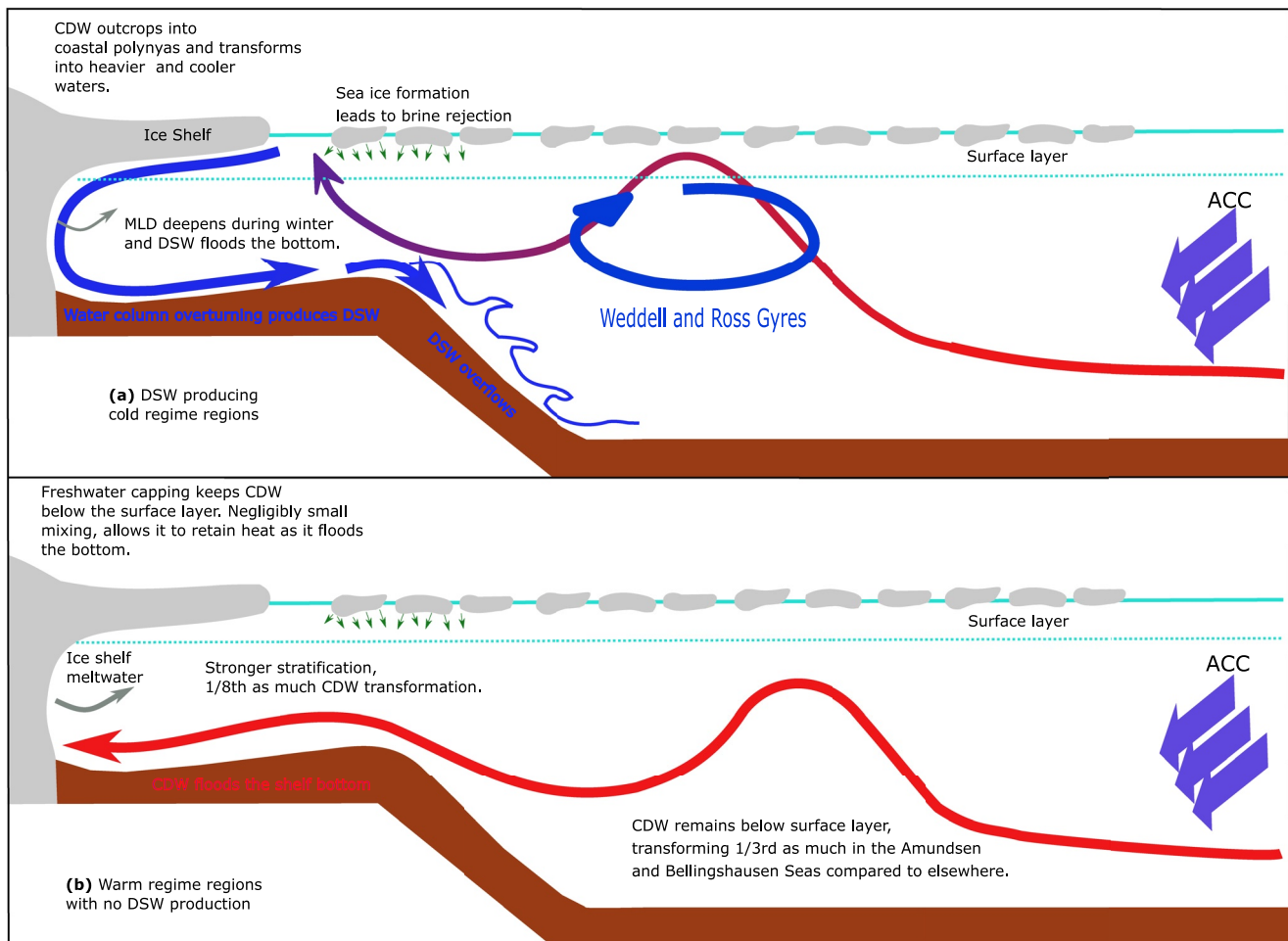
Figure 10. Illustration of processes influencing the watermass transformation of Circumpolar Deep Water (CDW) for the two main regimes found around Antarctica. In the cold regime regions (Weddell and Ross seas), the CDW transformation in subpolar gyres and on the continental shelves strongly limit the amount of heat reaching the ice shelves. In the warm regime regions (Amundsen and Bellingshausen seas), the absence of CDW transformation allows nearly unmodified warm deep water to reach the ice shelves and contributes to intense melting.

over the open ocean gyres are as important as the heat loss over the continental shelves. Further, the subpolar gyres and the continental shelves with convection act to transform CDW. The transformation over the continental shelves is positive, indicating the formation of denser waters, which implies an erosion of the stratification and a more barotropic flow. Wåhlin et al. (2020) show that the barotropic component of flow is blocked from entering sub-ice-shelf cavities at the ice shelf front.

Thus, the subpolar gyres and the continental shelves provide a "sheltering" effect against oceanic heating for the ice shelves in the Weddell and Ross Seas and along the East Antarctic coastline. In contrast, in the Amundsen and Bellingshausen Seas, which do not have any subpolar gyres, CDW intrudes on the continental shelf at depth, retaining its warm offshore properties, gains access to the base of ice shelves and elevates their basal melt rates, which in turn, in a positive-feedback loop, enhances the stratification of these seas, thereby inhibiting the mixing of CDW with surface waters.

The study raises further questions regarding the mixing that CDW may undergo under ice shelves. The model used here does not include ice shelf cavities, but these are regions where ice shelf meltwater mixes with CDW, resulting in the upwelling of CDW (Jenkins & Jacobs, 2008). Such mixing may modulate the formation of the freshwater cap in the Amundsen and Bellingshausen Seas. Further, this work provides only a time-averaged state of CDW properties in the Southern Ocean. There is potential for a future study that could focus on the interannual variability of CDW transport and transformation, and how interbasin transport of continental shelf waters affects stratification over Antarctic marginal seas.

Dinniman et al. ([2011](#)) and Morrison et al. ([2020](#)) showed that CDW onshore flow across the continental shelf break is higher in regions with high DSW offshore flows. Their hypotheses and our findings are that this onshore CDW flow is not associated with elevated bottom temperatures over the continental shelf because CDW transforms into cooler watermasses due to the enhanced diapycnal mixing in the subpolar gyres and due to the weak stratification and convection over the continental shelves. These findings reveal the two-way coupled nature of CDW–DSW interaction and indicate that the interaction could lead to one of three bottom temperature regimes—cold, intermediate, or warm—depending on the balance of forcings over the continental shelf (DSW formation) and the subpolar regions (stratification, and gyre driven upwelling).

Appendix A: Discretization of the Rates of Watermass Transformation

The rates of watermass transformation as defined in Equation [1](#) can be computed using model data on a grid using their discretized form,

$$\Omega(\sigma, t)_{i,j} = \frac{1}{\Delta\sigma} \sum_{k=1}^{N_z} \left(\Delta V_{i,j,k} \left(\frac{D\sigma}{Dt} \right)_{i,j,k} \delta(\sigma - \sigma_{i,j,k}) \right), \tag{A1}$$

with (i, j) the horizontal indices of a given grid cell, and k the vertical index. Here D/Dt is the material derivative operator, δV is the volume of the grid cell, σ is the density at the grid cell, N_z is the number of vertical levels from 0 to 700 m depth, and the discretized delta function δ is equal to $1/\Delta\sigma$ if $|x| \leq \Delta\sigma/2$, and zero otherwise.

The time-mean watermass transformation rates shown in the main manuscript are representative of the net transformation rates and hide the seasonal variations between summer (sea-ice melt period from December to February) and winter (sea-ice growth period from July to September), are shown in Figure S4 in Supporting Information [S1](#).

Data Availability Statement

All computer code, Supporting Information [S1](#), and some of the processed model fields used in this analysis are available in an open-access repository (Narayanan, [2021](#)). The complete model fields are available through the Southern Ocean State Estimate website (R. M. Mazloff, [2017](#)).

References

Abernathey, R. P., Cerovecki, I., Holland, P. R., Newsom, E., Mazloff, M., & Talley, L. D. (2016). Water-mass transformation by sea ice in the upper branch of the Southern Ocean overturning. *Nature Geoscience*, *9*(8), 596–601. https://doi.org/10.1038/ngeo2749

Adcroft, A., Hill, C., & Marshall, J. (1997). Representation of topography by shaved cells in a height coordinate ocean model. *Monthly Weather Review*, *125*(9), 2293–2315. https://doi.org/10.1175/1520-0493(1997)125%3C2293:ROTBSC%3E2.0.CO;2

Adusumilli, S., Fricker, H. A., Medley, B., Padman, L., & Siegfried, M. R. (2020). Interannual variations in meltwater input to the Southern Ocean from Antarctic ice shelves. *Nature Geoscience*, *13*(99), 616–620. https://doi.org/10.1038/s41561-020-0616-z

Argo. (2019). Argo float data and metadata from Global Data Assembly Centre (Argo GDAC)—Snapshot of Argo GDAC of July 8th 2019. https://doi.org/10.17882/42182#64916

Årthun, M., Nicholls, K. W., Makinson, K., Fedak, M. A., & Boehme, L. (2012). Seasonal inflow of warm water onto the southern Weddell Sea continental shelf, Antarctica. *Geophysical Research Letters*, *39*(17). https://doi.org/10.1029/2012GL052856

Bretherton, C. S., Widmann, M., Dymnikov, V. P., Wallace, J. M., & Bladé, I. (1999). The effective number of spatial degrees of freedom of a time-varying field. *Journal of Climate*, *12*(7), 1990–2009. https://doi.org/10.1175/1520-0442(1999)012⟨1990:TENOSD⟩2.0.CO;2

Chavanne, C. P., Heywood, K. J., Nicholls, K. W., & Fer, I. (2010). Observations of the Antarctic Slope Undercurrent in the southeastern Weddell Sea. *Geophysical Research Letters*, *37*(13). https://doi.org/10.1029/2010GL043603

Dee, D. P., Uppala, S. M., Simmons, A. J., Berrisford, P., Poli, P., Kobayashi, S., et al. (2011). The ERA-Interim reanalysis: Configuration and performance of the data assimilation system. *Quarterly Journal of the Royal Meteorological Society*, *137*(656), 553–597. https://doi.org/10.1002/qj.828

Dinniman, M. S., Klinck, J. M., & Smith, W. O., Jr. (2011). A model study of Circumpolar Deep Water on the West Antarctic Peninsula and Ross Sea continental shelves. *Deep Sea Research Part II: Topical Studies in Oceanography*, *58*(13–16), 1508–1523. https://doi.org/10.1016/j.dsr2.2010.11.013

Erickson, Z. K., Thompson, A. F., Cassar, N., Sprintall, J., & Mazloff, M. R. (2016). An advective mechanism for deep chlorophyll maxima formation in southern Drake Passage. *Geophysical Research Letters*, *43*(20), 10846–10855. https://doi.org/10.1002/2016GL070565

ETOPO1. (2009). ETOPO1 1 arc-minute global relief model. https://doi.org/10.7289/V5C8276M

Fenty, I., & Heimbach, P. (2013). Coupled sea ice–ocean-state estimation in the Labrador Sea and Baffin Bay. *Journal of Physical Oceanography*, *43*(5), 884–904. https://doi.org/10.1175/JPO-D-12-065.1

Forget, G., Campin, J.-M., Heimbach, P., Hill, C. N., Ponte, R. M., & Wunsch, C. (2015). ECCO version 4: An integrated framework for non-linear inverse modeling and global ocean state estimation. *Geoscientific Model Development*, *8*(10), 3071–3104. https://doi.org/10.5194/gmd-8-3071-2015

Fox-Kemper, B., & Menemenlis, D. (2008). Can large eddy simulation techniques improve mesoscale rich ocean models. *Ocean Modeling in an Eddying Regime*, *177*, 319–337. https://doi.org/10.1029/177GM19

Gaspar, P., Grégoris, Y., & Lefevre, J.-M. (1990). A simple eddy kinetic energy model for simulations of the oceanic vertical mixing: Tests at station Papa and Long-Term Upper Ocean Study site. *Journal of Geophysical Research*, *95*(C9), 16179–16193. https://doi.org/10.1029/JC095iC09p16179

Gille, S. T., McKee, D. C., & Martinson, D. G. (2016). Temporal changes in the Antarctic Circumpolar Current: Implications for the Antarctic continental shelves. *Oceanography*, *29*(4), 96–105. https://doi.org/10.5670/oceanog.2016.102

Good, S. A., Martin, M. J., & Rayner, N. A. (2013). EN4: Quality controlled ocean temperature and salinity profiles and monthly objective analyses with uncertainty estimates. *Journal of Geophysical Research: Oceans*, *118*(12), 6704–6716. https://doi.org/10.1002/2013JC009067

Groeskamp, S., Griffies, S. M., Iudicone, D., Marsh, R., Nurser, A. G., & Zika, J. D. (2019). The water mass transformation framework for ocean physics and biogeochemistry. *Annual Review of Marine Science*, *11*(1), 271–305. https://doi.org/10.1146/annurev-marine-010318-095421

Guo, G., Gao, L., & Shi, J. (2020). Modulation of Dense Shelf Water salinity variability in the western Ross Sea associated with the Amundsen Sea Low. *Environmental Research Letters*, *16*(1), 014004. https://doi.org/10.1088/1748-9326/abc995

Hammond, M. D., & Jones, D. C. (2016). Freshwater flux from ice sheet melting and iceberg calving in the Southern Ocean. *Geoscience Data Journal*, *3*(2), 60–62. https://doi.org/10.1002/gdj3.43

Hansen, J., Sato, M., Hearty, P., Ruedy, R., Kelley, M., Masson-Delmotte, V., et al. (2016). Ice melt, sea level rise and superstorms: Evidence from paleoclimate data, climate modeling, and modern observations that 2 °C global warming could be dangerous. *Atmospheric Chemistry and Physics*, *16*(6), 3761–3812. https://doi.org/10.5194/acp-16-3761-2016

Heywood, K. J., Naveira Garabato, A. C., Stevens, D. P., & Muench, R. D. (2004). On the fate of the Antarctic Slope Front and the origin of the Weddell Front. *Journal of Geophysical Research*, *109*(C6), C06021. https://doi.org/10.1029/2003JC002053

Hillenbrand, C.-D., Smith, J. A., Hodell, D. A., Greaves, M., Poole, C. R., Kender, S., et al. (2017). West Antarctic Ice Sheet retreat driven by Holocene warm water incursions. *Nature*, *547*(7661), 43–48. https://doi.org/10.1038/nature22995

Iudicone, D., Madec, G., Blanke, B., & Speich, S. (2008). The role of Southern Ocean surface forcings and mixing in the global conveyor. *Journal of Physical Oceanography*, *38*(7), 1377–1400. https://doi.org/10.1175/2008jpo3519.1

Jackett, D. R., & McDougall, T. J. (1997). A neutral density variable for the world's oceans. *Journal of Physical Oceanography*, *27*(2), 237–263. https://doi.org/10.1175/1520-0485(1997)027%3C0237:ANDVFT%3E2.0.CO;2

Jacobs, S. S., Jenkins, A., Giulivi, C. F., & Dutrieux, P. (2011). Stronger ocean circulation and increased melting under Pine Island Glacier ice shelf. *Nature Geoscience*, *4*(8), 519–523. https://doi.org/10.1038/ngeo1188

Jenkins, A., & Jacobs, S. (2008). Circulation and melting beneath George VI Ice Shelf, Antarctica. *Journal of Geophysical Research*, *113*(C4), C04013. https://doi.org/10.1029/2007JC004449

Jullion, L., Garabato, A. C. N., Bacon, S., Meredith, M. P., Brown, P. J., Torres-Valdés, S., et al. (2014). The contribution of the Weddell Gyre to the lower limb of the global overturning circulation. *Journal of Geophysical Research: Oceans*, *119*(6), 3357–3377. https://doi.org/10.1002/2013JC009725

Large, W. G., & Yeager, S. G. (2004). *Diurnal to decadal global forcing for ocean and sea-ice models: The data sets and flux climatologies*. National Center for Atmospheric Research Boulder. https://doi.org/10.5065/D6KK98Q6

Lewis, E., & Perkin, R. (1986). Ice pumps and their rates. *Journal of Geophysical Research*, *91*(C10), 11756–11762. https://doi.org/10.1029/JC091iC10p11756

Mazloff, M. R., Heimbach, P., & Wunsch, C. (2010). An eddy-permitting Southern Ocean state estimate. *Journal of Physical Oceanography*, *40*(5), 880–899. https://doi.org/10.1175/2009JPO4236.1

Mazloff, R. M. (2017). Southern ocean 1/12° model [Dataset]. SOCCOM. Retrieved from http://sose.ucsd.edu/

Morrison, A., Hogg, A. M., England, M. H., & Spence, P. (2020). Warm Circumpolar Deep Water transport toward Antarctica driven by local dense water export in canyons. *Science Advances*, *6*(18), eeav2516. https://doi.org/10.1126/sciadv.aav2516

Narayanan, A. (2021). Interaction of Circumpolar Deep Water with large-scale circulation and shelf water masses in the Southern Ocean [Software]. OSF. Retrieved from https://osf.io/f6tkr/

Narayanan, A., Gille, S. T., Mazloff, M., & Murali, K. (2019). Water mass characteristics of the Antarctic margins and the production and seasonality of Dense Shelf Water. *Journal of Geophysical Research: Oceans*, *124*(12), 9277–9294. https://doi.org/10.1029/2018JC014907

Ohshima, K. I., Fukamachi, Y., Williams, G. D., Nihashi, S., Roquet, F., Kitade, Y., et al. (2013). Antarctic Bottom Water production by intense sea-ice formation in the Cape Darnley polynya. *Nature Geoscience*, *6*(3), 235–240. https://doi.org/10.1038/ngeo1738

Olbers, D., Borowski, D., Völker, C., & Wölff, J.-O. (2004). The dynamical balance, transport and circulation of the Antarctic Circumpolar Current. *Antarctic Science*, *16*(4), 439–470. https://doi.org/10.1017/S0954102004002251

Orsi, A., Johnson, G., & Bullister, J. (1999). Circulation, mixing, and production of Antarctic Bottom Water. *Progress in Oceanography*, *43*(1), 55–109. https://doi.org/10.1016/S0079-6611(99)00004-X

Park, Y. H., Charriaud, E., & Fieux, M. (1998). Thermohaline structure of the Antarctic surface water/winter water in the Indian sector of the Southern Ocean. *Journal of Marine Systems*, *17*(1), 5–23. https://doi.org/10.1016/S0924-7963(98)00026-8

Pellichero, V., Sallée, J.-B., Chapman, C. C., & Downes, S. M. (2018). The Southern Ocean meridional overturning in the sea-ice sector is driven by freshwater fluxes. *Nature Communications*, *9*(1), 1789. https://doi.org/10.1038/s41467-018-04101-2

Petty, A. A., Feltham, D. L., & Holland, P. R. (2013). Impact of atmospheric forcing on Antarctic continental shelf water masses. *Journal of Physical Oceanography*, *43*(5), 920–940. https://doi.org/10.1175/JPO-D-12-0172.1

Piñones, A., Hofmann, E. E., Costa, D. P., Goetz, K., Burns, J. M., Roquet, F., et al. (2019). Hydrographic variability along the inner and mid-shelf region of the western Ross Sea obtained using instrumented seals. *Progress in Oceanography*, *174*, 131–142. https://doi.org/10.1016/j.pocean.2019.01.003

Ribeiro, N., Herraiz-Borreguero, L., Rintoul, S., McMahon, C., Hindell, M., Harcourt, R., & Williams, G. (2021). Warm modified Circumpolar Deep Water intrusions drive ice shelf melt and inhibit Dense Shelf Water formation in Vincennes Bay, East Antarctica. *Journal of Geophysical Research: Oceans*, *126*(8), e2020JC016998. https://doi.org/10.1029/2020JC016998

Rieger, N., Corral, A., Olmedo, E., & Turiel, A. (2021). Lagged teleconnections of climate variables identified via complex rotated maximum covariance analysis. *Journal of Climate*, *34*(24), 9861–9878. https://doi.org/10.1175/JCLI-D-21-0244.1

Rignot, E., Jacobs, S., Mouginot, J., & Scheuchl, B. (2013). Ice-shelf melting around Antarctica. *Science*, *341*(6143), 266–270. https://doi.org/10.1126/science.1235798

Roquet, F., Charrassin, J.-B., Marchand, S., Boehme, L., Fedak, M., Reverdin, G., & Guinet, C. (2011). Delayed-mode calibration of hydrographic data obtained from animal-borne satellite relay data loggers. *Journal of Atmospheric and Oceanic Technology*, *28*(6), 787–801. https://doi.org/10.1175/2010JTECHO801.1

Schmidtko, S., Heywood, K. J., Thompson, A. F., & Aoki, S. (2014). Multidecadal warming of Antarctic waters. *Science*, *346*(6214), 1227–1231. https://doi.org/10.1126/science.1256117

Semtner, A. J., Jr. (1976). A model for the thermodynamic growth of sea ice in numerical investigations of climate. *Journal of Physical Oceanography*, *6*(3), 379–389. https://doi.org/10.1175/1520-0485(1976)006%3C0379:AMFTTG%3E2.0.CO;2

Siegelman, L., Roquet, F., Mensah, V., Rivière, P., Pauthenet, E., Picard, B., & Guinet, C. (2019). Correction and accuracy of high and low resolution CTD data from animal borne instruments. *Journal of Atmospheric and Oceanic Technology*, *36*(5), 745–760. https://doi.org/10.1175/JTECH-D-18-0170.1

Silvano, A., Rintoul, S. R., Peña-Molino, B., Hobbs, W. R., van Wijk, E., Aoki, S., et al. (2018). Freshening by glacial meltwater enhances melting of ice shelves and reduces formation of Antarctic Bottom Water. *Science Advances*, *4*(4). https://doi.org/10.1126/sciadv.aap9467

SOCCOM. (2019). Southern ocean carbon and climate observations and modelling (SOCCOM). Retrieved from https://soccom.princeton.edu/

Stewart, A. L., & Thompson, A. F. (2012). Sensitivity of the ocean's deep overturning circulation to easterly Antarctic winds. *Geophysical Research Letters*, *39*(18). https://doi.org/10.1029/2012GL053099

Stewart, A. L., & Thompson, A. F. (2015). Eddy-mediated transport of warm Circumpolar Deep Water across the Antarctic shelf break. *Geophysical Research Letters*, *42*(2), 432–440. https://doi.org/10.1002/2014GL062281

St-Laurent, P., Klinck, J. M., & Dinniman, M. S. (2013). On the role of coastal troughs in the circulation of warm Circumpolar Deep Water on Antarctic shelves. *Journal of Physical Oceanography*, *43*(1), 51–64. https://doi.org/10.1175/JPO-D-11-0237.1

Talley, L. D. (2013). Closure of the global overturning circulation through the Indian, Pacific, and Southern Oceans: Schematics and transports. *Oceanography*, *26*(1), 80–97. https://doi.org/10.5670/oceanog.2013.07

Tamsitt, V., England, M. H., Rintoul, S. R., & Morrison, A. K. (2021). Residence time and transformation of warm Circumpolar Deep Water on the Antarctic continental shelf. *Geophysical Research Letters*, *48*(20), e2021GL096092. https://doi.org/10.1029/2021GL096092

Thoma, M., Jenkins, A., Holland, D., & Jacobs, S. (2008). Modelling Circumpolar Deep Water intrusions on the Amundsen Sea continental shelf, Antarctica. *Geophysical Research Letters*, *35*(18), L18602. https://doi.org/10.1029/2008GL034939

Thompson, A. F., Stewart, A. L., Spence, P., & Heywood, K. J. (2018). The Antarctic Slope Current in a changing climate. *Reviews of Geophysics*, *56*(4), 741–770. https://doi.org/10.1029/2018RG000624

Treasure, A. M., Roquet, F., Ansorge, I. J., Bester, M. N., Boehme, L., Bornemann, H., et al. (2017). Marine mammals exploring the oceans pole to pole: A review of the MEOP consortium. *Oceanography*, *30*(2), 132–138. https://doi.org/10.5670/oceanog.2017.234

Wåhlin, A. K., Steiger, N., Darelius, E., Assmann, K. M., Glessmer, M. S., Ha, H. K., et al. (2020). Ice front blocking of ocean heat transport to an Antarctic ice shelf. *Nature*, *578*(7796), 568–571. https://doi.org/10.1038/s41586-020-2014-5

Webb, D., Holmes, R., Spence, P., & England, M. (2019). Barotropic Kelvin wave-induced bottom boundary layer warming along the West Antarctic Peninsula. *Journal of Geophysical Research: Oceans*, *124*(3), 1595–1615. https://doi.org/10.1029/2018JC014227

Whitworth, T., III, Orsi, A. H., Kim, S.-J., Nowlin, W. D., Jr., & Locarnini, R. A. (1998). Water masses and mixing near the Antarctic Slope Front. In *Ocean, ice, and atmosphere: Interactions at the Antarctic continental margin* (pp. 1–27). American Geophysical Union (AGU). https://doi.org/10.1029/AR075p0001

Williams, G., Herraiz-Borreguero, L., Roquet, F., Tamura, T., Ohshima, K., Fukamachi, Y., et al. (2016). The suppression of Antarctic bottom water formation by melting ice shelves in Prydz Bay. *Nature Communications*, *7*(1), 12577. https://doi.org/10.1038/ncomms12577

Willmott, C. J., & Matsuura, K. (2005). Advantages of the mean absolute error (MAE) over the root mean square error (RMSE) in assessing average model performance. *Climate Research*, *30*(1), 79–82. https://doi.org/10.3354/cr030079

Wong, A., Keeley, R., Carval, T., & Argo Data Management Team (2020). Argo quality control manual for CTD and trajectory data [Computer software manual]. Argo. https://doi.org/10.13155/33951

Zhang, J., & Hibler, W. D., III. (1997). On an efficient numerical method for modeling sea ice dynamics. *Journal of Geophysical Research*, *102*(C4), 8691–8702. https://doi.org/10.1029/96JC03744